Depth-dependent crustal stress rotation and strength variation in the Charlevoix Seismic Zone (CSZ), Québec, Canada

Alessandro Verdecchia[1], John Onwuemeka[2], Yajing Liu[2], and Rebecca M. Harrington[1]

[1]Ruhr University Bochum
[2]McGill University

November 22, 2022

Abstract

Intraplate tectonic stress fields are complex due to the imprint of a long geological history. Here we use a new dataset of earthquake focal mechanism solutions and relocated events to investigate the relationship between regional stress, crustal strength, and seismicity in the Charlevoix Seismic Zone (CSZ), the most active seismic zone in eastern Canada. Our stress inversion shows that SHmax gradually rotates clockwise from approximately St. Lawrence River-parallel near the surface to river-perpendicular in the lower crust, as postglacial rebound stress becomes increasingly dominant at greater depth. The stress rotation occurs primarily between ˜13 and ˜26 km depth, where glacial rebound induced stress perturbation is further amplified by a "weaker" middle crust of an estimated apparent friction coefficient of ˜0.5. Finally, depth-dependent b-values confirm the rheological difference between upper and middle crust in the CSZ.

Depth-dependent crustal stress rotation and strength variation in the Charlevoix Seismic Zone (CSZ), Québec, Canada

A. Verdecchia[1], J. Onwuemeka[2], Y. Liu[2], and R. M. Harrington[1]

[1]Institute of Geology, Mineralogy and Geophysics, Ruhr-University Bochum, Bochum, Germany.

[2]Department of Earth and Planetary Sciences, McGill University, Montreal, Québec, Canada.

Corresponding author: Alessandro Verdecchia (alessandro.verdecchia@rub.de)

Key Points:

- Preexisting weaknesses in the CSZ amplify postglacial horizontal stresses and cause large clockwise stress rotations
- Stress rotation is further amplified in mid-crust due to low friction and semi-brittle behavior
- The frequency-magnitude distribution of earthquakes suggests an inverse relationship of *b*-value with differential stress in the upper crust

Abstract

Intraplate tectonic stress fields are complex due to the imprint of a long geological history. Here we use a new dataset of earthquake focal mechanism solutions and relocated events to investigate the relationship between regional stress, crustal strength, and seismicity in the Charlevoix Seismic Zone (CSZ), the most active seismic zone in eastern Canada. Our stress inversion shows that S_{Hmax} gradually rotates clockwise from approximately St. Lawrence River-parallel near the surface to river-perpendicular in the lower crust, as postglacial rebound stress becomes increasingly dominant at greater depth. The stress rotation occurs primarily between ~13 and ~26 km depth, where glacial rebound induced stress perturbation is further amplified by a “weaker” middle crust of an estimated apparent friction coefficient of ~0.5. Finally, depth-dependent *b*-values confirm the rheological difference between upper and middle crust in the CSZ.

Plain Language Summary

The occurrence of earthquakes in continent interiors is controlled by several geological and geophysical conditions which are often poorly known. High-resolution earthquake catalogs and information about faulting mechanisms are therefore key for recognizing and quantifying the crustal stress and strength conditions in these challenging regions. This study focuses on the Charlevoix Seismic Zone (CSZ), one of the most seismically active regions in eastern North America. By analyzing a new set of earthquake distribution and faulting data, we found that the combination between a “weak” fault zone and crustal stresses generated by postglacial rebound possibly controls the spatio-temporal distribution of earthquakes in the CSZ. In particular, the seismicity rate and faulting style in the CSZ strongly relate with the depth-dependent frictional and rheological properties of the crust.

1. Introduction

Crustal stress magnitude and orientation exhibits primary control on fault slip and earthquake rupture behavior. Because direct *in situ* stresses measurements are challenging and often restricted to the shallowest part of the upper crust, regional stress field orientation is typically inferred by indirect estimation, particularly at seismogenic depths. Stress inversion based on earthquake focal mechanism solutions (FMS) provide a robust tool to quantify the spatio-temporal distribution of stress orientation and relative magnitudes that are critical for studying the source mechanisms of plate boundary and intraplate seismicity (e.g., Hardebeck & Hauksson, 2001; Mazzotti & Townend, 2010). Moreover, results from stress inversions can be evaluated against the frequency-magnitude distribution of earthquakes to better understand the relationship between seismic activity, stress orientation, and crustal strength (Abolfathian et al., 2019). For example, *b*-values exhibit spatio-temporal variations that may be indicative of spatio-temporal changes in stress. Van Stiphout et al. (2009) found that higher *b*-value is associated with slab dehydration in the Alaskan subduction zone, which leads to pore pressure increases and subsequent fault strength reduction that promotes failure. Mori & Abercrombie (1997) studied the influence of earthquake hypocenters between 0 and 13 km from various dataset (**M** 2.0 - 5.5) in northern and southern in California, and found that decreasing heterogeneity in crustal materials with depth leads to *b*-value decreases. They interpreted rupture growth increases with lithostatic stress and decreasing heterogeneity to lead to an increase in propensity of larger earthquakes with depth as the crust becomes more homogeneous.

Intraplate tectonic settings pose specific challenges for quantifying crustal stress and strength conditions and their relation to earthquakes. In general, the relatively lower intraplate seismicity rates provide limited information about the geological and geophysical conditions for generating earthquakes, such as well-constrained earthquake rates or potential maximum magnitudes, which are key parameters for hazard assessment (Stein & Mazzotti, 2007 and references therein). Nevertheless, intraplate settings can experience infrequent, destructive earthquakes. The

Charlevoix Seismic Zone (CSZ) (Figure 1) along the St. Lawrence paleorift system in eastern Canada is one of the most seismically active intraplate settings, and has experienced five **M** 6+ earthquakes since the seventeenth century (Adams & Basham, 1991; Lamontagne, 1987), including a **M** 7.3 to 7.9 in Charlevoix in 1663 (Ebel, 2011). Structural inheritance related to the Grenville and Taconian orogeny, the coincident breakup of Rodinia and opening of the Iapetus Ocean, and late Ordovician to early Silurian meteorite impact causes extensive lithospheric-scale tectonic weakness within the paleorift system (Lemieux et al., 2003; Mazzotti & Gueydan, 2018; Rondot, 1971; Schmieder et al., 2019). The rifting associated with the Iapetus Ocean opening created the St. Lawrence valley system of normal faults that are presently under compressional stress conditions (Adams & Basham, 1991; Johnston, 1989). Seismic tomography and gravitational field modeling suggest that seismic velocity variations are dominated by the distribution of crustal fractures within the impact structure and material composition outside the impact structure. The crustal characteristics dictate distinctive spatial distributions of earthquake source properties, such as magnitudes, focal mechanisms, and static stress drop values (Onwuemeka et al., 2018; 2021). Postglacial rebound associated with glacial retreat following the Wisconsin glaciation (85 – 11 kyr) superimposes ambient stresses which possibly contribute to stress perturbations on critically stressed faults in the CSZ (Quinlan, 1984; Wu & Hasegawa, 1996). In particular, Mazzotti & Townend (2010) hypothesize that postglacial rebound in combination with a weak fault zone may explain the ~30° clockwise rotation of the maximum horizontal stress from shallow borehole measurements to those inferred from CSZ earthquake FM solutions. While the FMS-inferred stress orientations by Mazzotti & Townend (2010) may be representative of the entire region, the limited number of solutions (60) from their study make it difficult to estimate possible spatial variation of the stress orientation. In particular, depth-dependent stress variation would provide critical insights for understanding the rheological properties of the lithosphere, fault structures, and their influence on earthquake source processes, as demonstrated in other regional studies (Bokelmann & Beroza, 2000; Li et al., 2018).

In this study we take advantage of a new catalog of 161 FMS (**M** 1.5+) calculated using a full-waveform moment tensor inversion technique to investigate the spatial variations in stress field orientation with respect to the earthquake distribution in the CSZ. We combine FMS with existing data to determine the orientation and relative magnitudes of the principal stresses with particular focus on depth-dependent variations. We show the maximum horizontal stress rotates clockwise with depth from the near surface approximately river-parallel borehole breakout orientation toward roughly river-perpendicular maximum strain rate direction inferred in the lower crust. The stress rotation occurs primarily in the middle crust (~13-26 km), where the effect of postglacial rebound is amplified by a "weaker" crust with low frictional strength and semi-brittle rheology.

2. Data and Methods

We use a dataset of 1760 earthquakes (M_N -0.7 – 5.4; M_N is Nuttli magnitude (Nuttli, 1973)) that occurred in the CSZ between January 1988 and August 2017 (Figure 1a), with a ~ 2 years gap between 2010 and 2012 built from combining the relocated earthquake catalogs of Yu et al. (2016a) and Onwuemeka et al. (2018). We calculate the *b*-value and the magnitude of completeness (M_c) of the relocated catalog using the maximum likelihood method (Utsu, 1965) and Goodness-of-Fit test (Wiemer & Wyss, 2000), respectively, using the mean values of 1000 bootstrap runs and the 68% confidence intervals.

We apply the probabilistic earthquake source inversion framework *Grond* (Heimann et al., 2018) to perform full moment tensor inversion of 161 M 1.3+ events reported between April 2000 and February 2018. We use waveform data recorded by seven CNSN stations (CN network, operational since October 1994), six Quebec-Maine Transect campaign stations (X8 network, August 2012-August 2016), two USArray Transportable Array campaign stations (TA network, August 2013-July 2015;), and four temporary McGill University stations (MG network, since July 2015) in the Charlevoix area. Following Onwuemeka et al. (2018), we use the St. Lawrence River south shore velocity model of Lamontagne (1999) to precalculate Green's Functions (GF) for modeling synthetic seismograms. Text S1 details the moment tensor inversion. We augment our solutions with 64 additional FMS (63 FMS of events occurring between June 1974 and October 1997 and 1 FMS of the 1925 M 6.2 Charlevoix – Kamouraska event) of varying quality factors (27 A, 11 B, 24 C, and 2 D; quality factor decreases alphabetically) computed by Mazzotti & Townend (2010). We then use the combined 225 FM (Figure 1b) to invert for the principal stress orientations, stress ratio $R = (\sigma_1 - \sigma_2)/ (\sigma_1 - \sigma_3)$, and apparent friction coefficient (μ) through an iterative joint focal mechanism inversion (STRESSINVERSE, Vavryčuk, 2014). Following Abolfathian et al. (2019) we refer to μ as the apparent friction coefficient, which is calculated in the stress inversion procedure. A bootstrap resampling (500) of the original set of 225 FMS constrains the 95% confidence intervals. In addition, we determine the orientation of the maximum horizontal stress, S_{Hmax}, with the method of Lund & Townend (2007). Text S2 details the standard stress inversion procedure.

3. Results

3.1 Spatial variability of b-value in the CSZ

The estimated M_c and *b*-value for the entire catalog are1.86 and 0.96 (0.92 – 0.99), respectively (Figure S1a). The 1432 events located within the impact structure have calculated M_c of 1.92 and b-values of 1.06 (1.02 – 1.09), while M_c and *b*-values of the 328 events located outside the impact structure are 1.54 and 0.70 (0.67 – 0.72), respectively (Figure S1b, c). To avoid bias in *b*-value estimation due to changes in M_c (Hainzl, 2016), we also calculate *b*-values using a fixed M_c equal to the one estimated for the entire catalog (1.86). The resulting values of 1.05 (1.03 – 1.07) for the events within the impact crater, and 0.78 (0.75 – 0.81) for events outside are in agreement with results from Yu et al., (2016a).

Furthermore, we compute the depth-dependent variation of M_c and *b*-value using 50% overlapping windows of 300 events (Figure 2). Depth-dependent changes in *b*-value and M_c appear to follow a similar trend (Figure 2b, c). In order to increase the estimate robustness, we recalculate *b*-values at a fixed M_c (1.86) for each depth interval (Figure 2d). Figure 2d shows results from both the entire catalog (black points and line), and events within the impact structure (magenta points and line). The *b*-values of the entire catalog clearly decrease with depth from ~ 1.1 to ~ 0.9 until approximately 12 km, followed by a brief rebound to ~ 1.0 for about 1 km, before returning to ~ 0.9 at greater depth. Events within the impact structure show *b*-values similar to the entire catalog until ~10 km depth, followed by a sudden increase with depth that peaks at ~1.2 at ~ 12.5 km. Between ~12.5 km and 15 km, *b*-values are similar between the two groups. Below ~15 km, the events within the impact zone exhibit higher *b*-values relative to the full catalog, although the estimates are less well-constrained due to the decrease of seismicity with depth (Figure 2a). The strong contrast in the *b*-value-depth variation between the two event populations likely results from the fact that seven of eight $M_N \geq 4$ earthquakes in the full catalog occurred outside the impact structure (Figure 2d), causing a strong statistical bias toward the larger magnitude events in the *b*-value estimate.

3.2 Focal mechanisms and moment tensor inversion

The majority of the earthquakes exhibit reverse-faulting kinematics (Figure 1b) consistent with reverse-sense reactivation of pre-existing Iapetus normal faults (e.g., Mazzotti & Townend, 2010; Onwuemeka et al., 2018). The extensive damage and relative higher fault/fracture density produced by the meteorite impact likely explain the higher diversity of FMS within the impact structure relative to other locations in the CSZ (Yu et al., 2016a).

Stress inversion results of the 225 FMs produce a maximum principal stress (σ_1) with a mean azimuth of 93° (Figure 1b), a roughly vertical minimum principal stress (σ_3), and intermediate principle stress (σ_2) with a mean azimuth of 184°. The estimated S_{Hmax} has a mean azimuth of 90.7°, which represents a clockwise rotation from the regional S_{Hmax} of 54° determined from borehole breakout studies (Mazzotti & Townend, 2010). Stress ratios R range between 0.26 and 0.56 with mean value of 0.41.

We evaluate the stress variation with depth by inverting for the principle-stress orientations in subset groups of 75 events overlapping by 60 events. We also invert for the maximum horizontal stress (S_{Hmax}), the stress ratio (R), and apparent friction coefficient (μ) within subsets (Figure 3). The results show a depth-dependent clockwise rotation of both σ_1 and σ_2 (Figure 3a, b). Mean values of σ_1 and σ_2 remain constant down to ~12.5 km within the 95% confidence intervals, with the largest stress rotation of σ_1 from azimuth ~ 80° to 110° and σ_2 from ~ 170° to 200° between ~12.5 and ~16 km depth. The inversion results show no additional stress rotation below ~16 km. In addition to the azimuth rotation of σ_1 and σ_2, the σ_1 plunge rotates from near-horizontal (~5°) to a shallow dip angle (~ 15°) at ~15 km depth (Figure 3c). Our results also show a decreasing trend with depth of both the R value from 0.7 at shallow depths to 0.25 at ~16 km and μ from 0.8 to 0.45 over the same depth range (Figure 3d, e). Finally, the results show a total clockwise rotation of S_{Hmax} of ~30° (82.5° to 111.8°) between shallow and deeper FMS (consistent with the σ_1 and σ_2 azimuthal rotations) and a total clockwise rotation of ~58° from the regional S_{Hmax} of 54° determined from borehole breakouts (Mazzotti & Townend, 2010) (Figure 3f).

4. Discussion

The S_{Hmax} orientation from borehole breakouts in eastern Canada suggests that a roughly NE – SW compression drives stress perturbation. Under a NE – SW compressive stress regime, Iapetan faults in the CSZ are not optimally-oriented for thrust faulting, and therefore require an additional perturbation of stress orientation to explain the prevalent thrust and reverse – oblique kinematics presently observed. "Weak" faults are a plausible cause for reactivation of non-optimally-oriented faults. Explanations for fault weakening include weak fault materials (clay-rich gauge) (Ikari et al., 2009), dynamic slip weakening and shear heating (Di Toro et al., 2006; Wibberley & Shimamoto, 2005), damage-induced changes in elastic properties (high fracture density) (Faulkner et al., 2006), and elevated pore fluid pressure (Byerlee, 1990).

Previous studies in eastern North America have proposed that postglacial isostatic rebound stresses following the Wisconsin glaciation (85 - 11 kyr) concentrate on faults by localized weaknesses (e.g., dense fracture networks) (e.g., Mazzotti & Townend, 2010; Wu & Hasegawa, 1996). Such stress concentrations on pre-existing zones of weakness may be the most probable source of stress perturbation and driving mechanism of the observed stress rotation. Although the magnitude of post-glacial isostatic rebound stresses are on the order of kPa, localized weaknesses within the highly fractured Charlevoix impact structure may locally enhance stresses. Tarayoun et al. (2018) found that localized structural inheritance amplifies surface strain across St. Lawrence Valley, suggesting that post-glacial isostatic rebound stresses causes significant stress perturbations in structurally weak zones.

The stress orientation observed here (Figure 1b) agrees with previous work. For example, Mazzotti & Townend (2010) found that S_{Hmax} is rotated by up to 47° (when considering the south-eastern cluster) in the CSZ with respect to the borehole breakout measurements. We note that the 64 of the FMS common to this study and Mazzotti & Townend (2010) make up less than 30 % of our dataset, and would unlikely bias our results. Similar clockwise S_{Hmax} rotations of 44° and 49° are reported for the Lower Saint Lawrence Seismic Zone (SLZ) north of the CSZ, respectively, by Mazzotti & Townend (2010) and Plourde & Nedimović (2021). Furthermore, Plourde & Nedimović (2021) also observed a clockwise rotation of ~ 49º of $\sigma_1$with depth in the LSZ, mostly inferred from mid-crustal depths. Similarly, our results show the largest clockwise rotation below ~13 km (Figures 3, and 4), which roughly represents the transition from upper to middle crust in the CSZ (Laske et al., 2013). The pronounced stress rotation observed in both the LSZ and CSZ are consistent with a "weaker" middle crust in both seismic zones. Mazzotti & Townend (2010) also observed that the largest S_{Hmax} rotation inferred from the cluster of events located southeast of the Saint-Laurent fault (Figure S2) relative to the cluster to the northwest. The difference can be explained by the depth-dependent rotation observed in this study, namely, the larger number of shallow events in the northern cluster (0 – 7 km) (Figure S2) results in a smaller stress rotation, whereas the relatively deeper southern cluster reflects the deeper, hence larger stress rotation.

The apparent friction coefficient (μ) calculated by the stress inversion also supports the "weaker" middle crust hypothesis, with highest values of μ (0.65 – 0.8) in the upper crust and lower relative values in the middle crust (0.45 – 0.6) (Figure 3e). A decrease in μ with depth would also explain the decrease in *R* (Figure 3d). The differential stress ($\sigma_1 - \sigma_3$) for thrust faulting can be expressed as follows (Sibson, 1974):

$$(\sigma_1 - \sigma_3) = (F\text{-}1)\, \rho g z\, (1\text{-}\lambda)$$

where $F = [(1+\mu^2)^{1/2} + \mu]^2$, ρ is the average crustal density, g is the gravitational acceleration, z is the depth, and $\lambda = P_f/\rho g z$ is the pore fluid factor, with P_f being pore fluid pressure. For thrust faulting $\sigma_3 = (1\text{-}\lambda)\, \rho g z$ (vertical stress), and $\sigma_1 = F\sigma_3$ (maximum horizontal stress), making σ_1 dependent on the friction coefficient (μ). Therefore, a decrease in μ will result in a decrease of both $\sigma_1 - \sigma_2$ and $\sigma_1 - \sigma_3$, and a subsequent decrease in *R*. However, the previous statement is only valid if both σ_2 and σ_3 are not affected by the change of μ.

Similar to the stress inversion results, depth-dependent *b*-values also show a significant change at the upper – middle crust boundary (12 km - 13 km) (Figure 2d). The *b*-values clearly decrease with depth until ~12 km and start increasing again following a variable trend. We evaluate possible effects of using M_N in our calculations, and convert M_N to M_W following Bent (2011). Figure S3 shows the M_W depth-dependent *b*-values follow a similar trend to M_N values (Figure 2). The inverse depth and *b*-value relationship observed in the upper crust of the CSZ is consistent with of Amitrano (2003) and Spada et al., (2013), both of whom observed decreasing *b*-values with increasing confining pressure and differential stress. Spada et al. (2013) also suggested that the change in the monotonic trend of *b*-value may reflect the location of the brittle-ductile transition. However, the observed trend reversal in *b*-value at ~ 12.5 km (Figure 2) may not reflect the brittle-ductile transition where seismicity typically diminishes with depth. Rather, seismicity here peaks around 12.5 km and remains abundant down to ~ 22 km (Figure 2a). Therefore, we hypothesize that upper – middle crust boundary located at ~ 12.5 km may instead represent a transition from a brittle behavior of the upper crust to a semi-brittle behavior of the middle crust, where brittle and ductile mechanisms coexist or alternate. The transition to a fully ductile regime likely occurs at ~ 26 km depth at the limit between middle and lower crust (Figure 4).

The discussion in the preceding paragraph accounts for all the events in the catalog. The significantly higher *b*-values between 10 km and 13 km within the impact structure support the presence of a locally highly fractured and weak upper crust (Yu et al., 2016a). The higher local *b*-values are particularly important for probabilistic seismic hazard assessment, given the implications on the frequency of possible future large earthquakes implied by *b*-values. Our results suggest a relatively higher seismic hazard outside the impact structure, when solely based on *b*-values. However, Yu et al. (2016a) interpreted the seismic moment deficit within the impact structure could imply a higher seismic hazard, if the moment deficit is the manifestation of locked faults storing accumulated strain energy. The authors also suggested that aseismic creep and strain release might hinder significant strain energy accumulation. However, the overall low geodetic strain rates in this area (Mazzotti & Adams, 2005; Sella et al., 2007) make it challenging to evaluate which of the above two scenarios is more plausible.

Figure 4 provides a conceptual framework of the crustal rheological structure in the CSZ interpreted from the results of this work. The mostly reverse faulting kinematics inferred from FM solutions in the CSZ (Figure 1b) are consistent with the horizontal compressional stress induced by the postglacial unloading following the Wisconsin glaciation (85 – 11 kyr) (Figure 4b) that is likely amplified by pre-existing structural weakness. The stress inversion results, in particular the depth-variable maximum horizontal stress S_{Hmax}, clearly depict systematic clockwise rotation from the NE-SW orientation inferred from shallow borehole measurements (~ parallel to the St Lawrence River) toward a NW-SE orientation (~ perpendicular to the SLR). The rotated NW-SE S_{Hmax} direction is consistent with maximum strain predicted by Glacial Isostatic Adjustment (GIA) models (Peltier et al., 2015). The largest S_{Hmax} rotation of up to ~ 60° from borehole breakouts is reached at mid-crustal depths ~ 20-26 km, where seismicity ceases. No earthquake FMS are available for stress inversion at greater depth, however, it is plausible that the clockwise rotation continues to approach the GIA estimated strain direction (Figure 4c). The large rotation is possibly due to a significant change in rheological and frictional properties of the middle crust as suggested by the depth-dependent b-value and μ variations (Figure 4d). Based on the above interpretations, we hypothesize a rheological profile including a brittle upper crust, a semi-brittle middle crust, and a ductile lower crust (Figure 4d). Finally, the rotation of the σ_1 plunge from near-horizontal (~5°) at the upper crust to shallowly dipping (~15°) at middle crust may reflect the initiation of the gradual transition with depth from a compressional (σ_1 horizontal) to an extensional regime (σ_1 vertical), as is expected under the influence of postglacial rebound (Figure 4a, 4b). Similar to the S_{Hmax} rotation, our stress inversion results can only capture the initial phase of σ_1 plunge rotation (due to the depth limits of seismicity) that likely continues with depth.

Several studies have shown that large earthquakes may produce temporal principal stress rotations in different tectonic settings (Hardebeck & Okada, 2018; Yu et al., 2016b). Here, we use the software Coulomb 3.4 (Toda et al., 2011) to test the extent to which the 1663 M 6+ (Ebel, 2011) event influences the regional stress orientation (Text S3 for details). Our results (Figure S4) show that significant stress rotation occurs within the context of low background differential stress. However, independent of the differential stress, none of the modeled cases explored here accurately represent the present state of stress in the CSZ (Figure 1b). In addition, regional stresses are expected to return to their pre-mainshock orientation within a few months to years (Hardebeck, 2012; Hardebeck & Okada, 2018). Therefore, stress enhancement due to localized weakness, post-glacial isostatic rebound, and ridge-push forces, must be invoked to adequately quantify higher seismic hazard in intraplate seismic zones (e.g., CSZ) in eastern North America.

5. Conclusions

We combine a methodology based on the stress inversion of 225 FMS with the frequency-magnitude distribution properties of earthquakes to investigate the spatial variation of stress field and crustal strength in the CSZ. Our results show that:

- The ~ 40° clockwise rotations of S_{Hmax} obtained from the inversion of the entire FMS catalog supports the hypothesis that pre-existing weaknesses in the CSZ amplify postglacial horizontal stresses.

- The large S_{Hmax} rotation below ~13 km depth is consistent with variable rheological and frictional properties of the middle crust, suggesting low friction coefficient and semi-brittle behavior, which further amplify postglacial rebound stresses.
- The monotonic decrease of *b*-value with depth in the upper ~ 13 km suggest an inverse relationship with differential stress in the upper crust. The relationship becomes insignificant in the middle crust due to its differing rheology.
- Historical large earthquakes do not significantly affect the present-day stress state in the CSZ.

Acknowledgements

We thank Pierre Archambault, Maurice Lamontagne, and Alain Tremblay for their assistance in the deployment and maintenance of the McGill stations in Charlevoix. This work is supported by the Team Research Program of the Fonds de Recherche du Québec - Nature et Technologies (PR-191259), and the Natural Sciences and Engineering Research Council of Canada (NSERC) Discovery Grant (RGPIN-2018-05389).

Open Research

The relocated catalog and the focal mechanisms solutions from this work are available in the Zenodo data repository (https://doi.org/10.5281/zenodo.6786234).

References

Abolfathian, N., Martínez-Garzón, P., & Ben-Zion, Y. (2019). Spatiotemporal Variations of Stress and Strain Parameters in the San Jacinto Fault Zone. *Pure and Applied Geophysics*, *176*(3), 1145–1168. https://doi.org/10.1007/s00024-018-2055-y

Adams, J., & Basham, P. (1991). The seismicity and seismotectonics of eastern Canada. https://doi.org/10.1130/DNAG-CSMS-NEO.261

Amitrano, D. (2003). Brittle-ductile transition and associated seismicity: Experimental and numerical studies and relationship with the b value. *Journal of Geophysical Research: Solid Earth*, *108*(B1). https://doi.org/10.1029/2001JB000680

Bent, A. L. (2011). Moment Magnitude (Mw) Conversion Relations for Use in Hazard Assessment in Eastern Canada. *Seismological Research Letters*, *82*(6), 984–990. https://doi.org/10.1785/gssrl.82.6.984

Bokelmann, G. H. R., & Beroza, G. C. (2000). Depth-dependent earthquake focal mechanism orientation: Evidence for a weak zone in the lower crust. *Journal of Geophysical Research: Solid Earth*, *105*(B9), 21683–21695. https://doi.org/10.1029/2000JB900205

Byerlee, J. (1990). Friction, overpressure and fault normal compression. *Geophysical Research Letters*, *17*(12), 2109–2112. https://doi.org/10.1029/GL017i012p02109

Di Toro, G., Hirose, T., Nielsen, S., Pennacchioni, G., & Shimamoto, T. (2006). Natural and Experimental Evidence of Melt Lubrication of Faults During Earthquakes. *Science*, *311*(5761), 647–649. https://doi.org/10.1126/science.1121012

Ebel, J. E. (2011). A New Analysis of the Magnitude of the February 1663 Earthquake at Charlevoix, QuebecA New Analysis of the Magnitude of the February 1663 Earthquake at Charlevoix, Quebec. *Bulletin of the Seismological Society of America*, *101*(3), 1024–1038. https://doi.org/10.1785/0120100190

Faulkner, D. R., Mitchell, T. M., Healy, D., & Heap, M. J. (2006). Slip on “weak” faults by the rotation of regional stress in the fracture damage zone. *Nature*, *444*(7121), 922–925. https://doi.org/10.1038/nature05353

Hainzl, S. (2016). Rate-Dependent Incompleteness of Earthquake Catalogs. *Seismological Research Letters*, *87*(2A), 337–344. https://doi.org/10.1785/0220150211

Hardebeck, J. L., & Hauksson, E. (2001). Crustal stress field in southern California and its implications for fault mechanics. *Journal of Geophysical Research: Solid Earth*, *106*(B10), 21859–21882. https://doi.org/10.1029/2001JB000292

Hardebeck, J. L., & Okada, T. (2018). Temporal Stress Changes Caused by Earthquakes: A Review. *Journal of Geophysical Research: Solid Earth*, *123*(2), 1350–1365. https://doi.org/10.1002/2017JB014617

Heimann, S., Isken, M., Kühn, D., Sudhaus, H., Steinberg, A., Daout, S., et al. (2018). Grond - A probabilistic earthquake source inversion framework (Version 1.0) [Application/octet-stream,application/octet-stream,application/octet-stream,application/octet-stream,application/octet-stream]. GFZ Data Services. https://doi.org/10.5880/GFZ.2.1.2018.003

Ikari, M. J., Saffer, D. M., & Marone, C. (2009). Frictional and hydrologic properties of clay-rich fault gouge. *Journal of Geophysical Research: Solid Earth*, *114*(B5). https://doi.org/10.1029/2008JB006089

Johnston, A. C. (1989). The Seismicity of 'Stable Continental Interiors.' In S. Gregersen & P. W. Basham (Eds.), *Earthquakes at North-Atlantic Passive Margins: Neotectonics and Postglacial Rebound* (pp. 299–327). Dordrecht: Springer Netherlands. https://doi.org/10.1007/978-94-009-2311-9_18

Lamontagne, M. (1987). Seismic activity and structural features in the Charlevoix region, Quebec. *Canadian Journal of Earth Sciences*, *24*(11), 2118–2129. https://doi.org/10.1139/e87-202

Lamontagne, M. (1999, January 1). *Rheological and geological constraints on the earthquake distribution in the Charlevoix Seismic Zone, Quebec, Canada*. *Ph.D. Thesis*. Retrieved from https://ui.adsabs.harvard.edu/abs/1999PhDT

Lemieux, Y., Tremblay, A., & Lavoie, D. (2003). Structural analysis of supracrustal faults in the Charlevoix area, Quebec: relation to impact cratering and the St-Laurent fault system. *Canadian Journal of Earth Sciences*, *40*(2), 221–235. https://doi.org/10.1139/e02-046

Li, D., McGuire, J. J., Liu, Y., & Hardebeck, J. L. (2018). Stress rotation across the Cascadia megathrust requires a weak subduction plate boundary at seismogenic depths. *Earth and Planetary Science Letters*, *485*, 55–64. https://doi.org/10.1016/j.epsl.2018.01.002

Lund, B., & Townend, J. (2007). Calculating horizontal stress orientations with full or partial knowledge of the tectonic stress tensor. *Geophysical Journal International*, *170*(3), 1328–1335. https://doi.org/10.1111/j.1365-246X.2007.03468.x

Mazzotti, S., & Adams, J. (2005). Rates and uncertainties on seismic moment and deformation in eastern Canada. *Journal of Geophysical Research: Solid Earth*, *110*(B9). https://doi.org/10.1029/2004JB003510

Mazzotti, S., & Gueydan, F. (2018). Control of tectonic inheritance on continental intraplate strain rate and seismicity. *Tectonophysics*, *746*, 602–610. https://doi.org/10.1016/j.tecto.2017.12.014

Mazzotti, S., & Townend, J. (2010). State of stress in central and eastern North American seismic zones. *Lithosphere*, *2*(2), 76–83. https://doi.org/10.1130/L65.1

Mori, J., & Abercrombie, R. E. (1997). Depth dependence of earthquake frequency-magnitude distributions in California: Implications for rupture initiation. *Journal of Geophysical Research: Solid Earth*, *102*(B7), 15081–15090. https://doi.org/10.1029/97JB01356

Nuttli, O. W. (1973). Seismic wave attenuation and magnitude relations for eastern North America. *Journal of Geophysical Research (1896-1977)*, *78*(5), 876–885. https://doi.org/10.1029/JB078i005p00876

Onwuemeka, J., Liu, Y., & Harrington, R. M. (2021). Crustal Velocity Variations and Constraints on Material Properties in the Charlevoix Seismic Zone, Eastern Canada. *Journal of Geophysical Research: Solid Earth*, *126*(7), e2020JB020918. https://doi.org/10.1029/2020JB020918

Onwuemeka, J., Liu, Y., & Harrington, R. M. (2018). Earthquake Stress Drop in the Charlevoix Seismic Zone, Eastern Canada. *Geophysical Research Letters*, *45*(22), 12,226-12,235. https://doi.org/10.1029/2018GL079382

Peltier, W. R., Argus, D. F., & Drummond, R. (2015). Space geodesy constrains ice age terminal deglaciation: The global ICE-6G_C (VM5a) model. *Journal of Geophysical Research: Solid Earth*, *120*(1), 450–487. https://doi.org/10.1002/2014JB011176

Plourde, A. P., & Nedimović, M. R. (2021). Earthquake Depths, Focal Mechanisms, and Stress in the Lower St. Lawrence Seismic Zone. *Seismological Research Letters*, *92*(4), 2562–2572. https://doi.org/10.1785/0220200429

Quinlan, G. (1984). Postglacial rebound and the focal mechanisms of eastern Canadian earthquakes. *Canadian Journal of Earth Sciences*, *21*(9), 1018–1023. https://doi.org/10.1139/e84-106

Rondot, J. (1971). Impactite of the Charlevoix Structure, Quebec, Canada. *Journal of Geophysical Research*, *76*(23), 5414–5423. https://doi.org/10.1029/JB076i023p05414

Schmieder, M., Shaulis, B. J., Lapen, T. J., Buchner, E., & Kring, D. A. (2019). In situ U–Pb analysis of shocked zircon from the Charlevoix impact structure, Québec, Canada. *Meteoritics & Planetary Science*, *54*(8), 1808–1827. https://doi.org/10.1111/maps.13315

Sella, G. F., Stein, S., Dixon, T. H., Craymer, M., James, T. S., Mazzotti, S., & Dokka, R. K. (2007). Observation of glacial isostatic adjustment in “stable” North America with GPS. *Geophysical Research Letters*, *34*(2). https://doi.org/10.1029/2006GL027081

Sibson, R. H. (1974). Frictional constraints on thrust, wrench and normal faults. *Nature*, *249*(5457), 542–544. https://doi.org/10.1038/249542a0

Spada, M., Tormann, T., Wiemer, S., & Enescu, B. (2013). Generic dependence of the frequency-size distribution of earthquakes on depth and its relation to the strength profile of the crust. *Geophysical Research Letters*, *40*(4), 709–714. https://doi.org/10.1029/2012GL054198

Stein, S., & Mazzotti, S. (2007). Continental Intraplate Earthquakes: Science, Hazard, and Policy Issues. https://doi.org/10.1130/SPE425

van Stiphout, T., Kissling, E., Wiemer, S., & Ruppert, N. (2009). Magmatic processes in the Alaska subduction zone by combined 3-D b value imaging and targeted seismic tomography. *Journal of Geophysical Research: Solid Earth*, *114*(B11). https://doi.org/10.1029/2008JB005958

Tarayoun, A., Mazzotti, S., Craymer, M., & Henton, J. (2018). Structural Inheritance Control on Intraplate Present-Day Deformation: GPS Strain Rate Variations in the Saint Lawrence Valley, Eastern Canada. *Journal of Geophysical Research: Solid Earth*, *123*(8), 7004–7020. https://doi.org/10.1029/2017JB015417

Toda, S., Stein, R. S., Sevilgen, V., & Lin, J. (2011). *Coulomb 3.3 Graphic-rich deformation and stress-change software for earthquake, tectonic, and volcano research and teaching-user guide* (USGS Numbered Series No. 2011–1060). *Coulomb 3.3 Graphic-rich deformation and stress-change software for earthquake, tectonic, and volcano research and teaching-user guide* (Vol. 2011–1060). Reston, VA: U.S. Geological Survey. https://doi.org/10.3133/ofr20111060

Utsu, T. (1965). A method for determining the value of. *Geophys. Bull. Hokkaido Univ.*, *13*, 99–103.

Vavryčuk, V. (2014). Iterative joint inversion for stress and fault orientations from focal mechanisms. *Geophysical Journal International*, *199*(1), 69–77. https://doi.org/10.1093/gji/ggu224

Wibberley, C. A. J., & Shimamoto, T. (2005). Earthquake slip weakening and asperities explained by thermal pressurization. *Nature*, *436*(7051), 689–692. https://doi.org/10.1038/nature03901

Wiemer, S., & Wyss, M. (2000). Minimum Magnitude of Completeness in Earthquake Catalogs: Examples from Alaska, the Western United States, and Japan. *Bulletin of the Seismological Society of America*, *90*(4), 859–869. https://doi.org/10.1785/0119990114

Wu, P., & Hasegawa, H. S. (1996). Induced stresses and fault potential in eastern Canada due to a realistic load: a preliminary analysis. *Geophysical Journal International*, *127*(1), 215–229. https://doi.org/10.1111/j.1365-246X.1996.tb01546.x

Yu, H., Liu, Y., Harrington, R. M., & Lamontagne, M. (2016). Seismicity along St. Lawrence Paleorift Faults Overprinted by a Meteorite Impact Structure in Charlevoix, Québec, Eastern Canada. *Bulletin of the Seismological Society of America*, *106*(6), 2663–2673. https://doi.org/10.1785/0120160036

Yu, H., Zhao, L., Liu, Y., Ning, J., Chen, Q.-F., & Lin, J. (2016). Stress adjustment revealed by seismicity and earthquake focal mechanisms in northeast China before and after the 2011 Tohoku-Oki earthquake. *Tectonophysics*, *666*, 23–32. https://doi.org/10.1016/j.tecto.2015.10.009

Figure captions

Figure 1. Seismicity in the Charlevoix Seismic Zone (CSZ). (a) Map of relocated earthquakes that occurred between January 1988 and August 2017. Events are color-coded by hypocentral depth. (b) Focal mechanism solutions (FMS) used in this study with the lower-right inset showing the results of the stress inversion from all the FMS. Solid black lines indicate known faults (Lamontagne, 1999; Rondot, 1971). Dashed circles indicate inner and outer boundaries of the meteorite impact structure. Black arrows indicate orientation of maximum horizontal stress from borehole breakouts.

Figure 2. Magnitude-frequency distribution of relocated earthquakes in the CSZ. (a) Distribution of earthquakes with depth. (b) Depth-dependent variation of magnitude of completeness (M_c) calculated using moving windows of 300 events with 150-event overlap. (c) Depth-dependent *b*-value calculated using M_c in (b). (d) Depth-dependent *b*-value variation of using a fixed M_c = 1.86. Black points represent *b*-values for the entire catalog, magenta points indicate *b*-values for

events within the impact structure. Grey bars indicate distribution of $M_N \geq 4$ events in the entire catalog (light) and within the events located inside the impact structure.

Figure 3. Depth-dependent variation of (a) σ_1 azimuth, (b) σ_2 azimuth, (c) σ_1 and σ_2 plunge, (d) stress ratio, and (e) apparent friction coefficient in moving windows of 75 events, overlapping by 15 events. Vertical lines represent depth range of the FMS used in each window, horizontal lines indicate 95% confidence interval. (f) Polar plots of specific stress inversions denoted by numbers (1-3). Black solid lines represent the orientation of the maximum horizontal stress (S_{Hmax}), with black dashed lines indicating 95% confidence interval limits of the. Grey solid lines represent the S_{Hmax} orientation from borehole breakouts (Mazzotti & Townend, 2010).

Figure 4. Schematic NW-SE cross section showing the expected horizontal stress distribution in the lithosphere during (a) glacial loading and (b) postglacial unloading following Wisconsin glaciation (85-11 kyr). (c) Conceptual model showing crustal depth-dependent clockwise rotation of maximum horizontal stress (S_{Hmax}) in the CSZ calculated here (black arrows) compared to S_{Hmax} from borehole breakouts data (grey arrows), and maximum horizontal strain direction from GIA modeling (Peltier et al., 2015). (d) Hypothetical rheological profile of the crust (solid lines color-coded by section of the crust) in the CSZ based on the distribution of earthquakes (grey histogram), *b*-value (dashed red line), apparent friction coefficient (μ) (dashed black line). Black arrows show the calculated rotation of the σ_1 plunge interpreted as possible transition to an extensional regime approaching the neutral plane (a, b). Vertical and horizontal axis do not have the same scale.

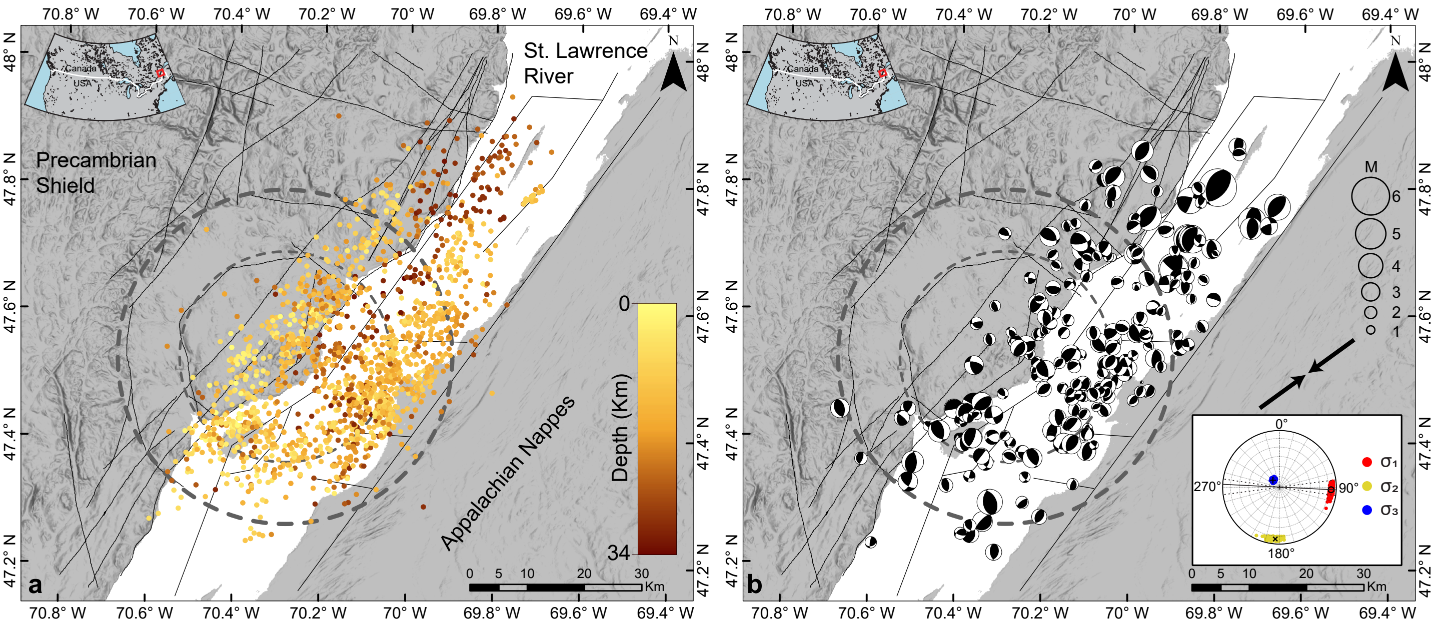

Figure 1. Seismicity in the Charlevoix Seismic Zone (CSZ). (a) Map of relocated earthquakes that occurred between January 1988 and August 2017. Events are color-coded by hypocentral depth. (b) Focal mechanism solutions (FMS) used in this study with the lower-right inset showing the results of the stress inversion from all the FMS. Solid black lines indicate known faults (Lamontagne, 1999; Rondot, 1971). Dashed circles indicate inner and outer boundaries of the meteorite impact structure. Black arrows indicate orientation of maximum horizontal stress from borehole break-outs.

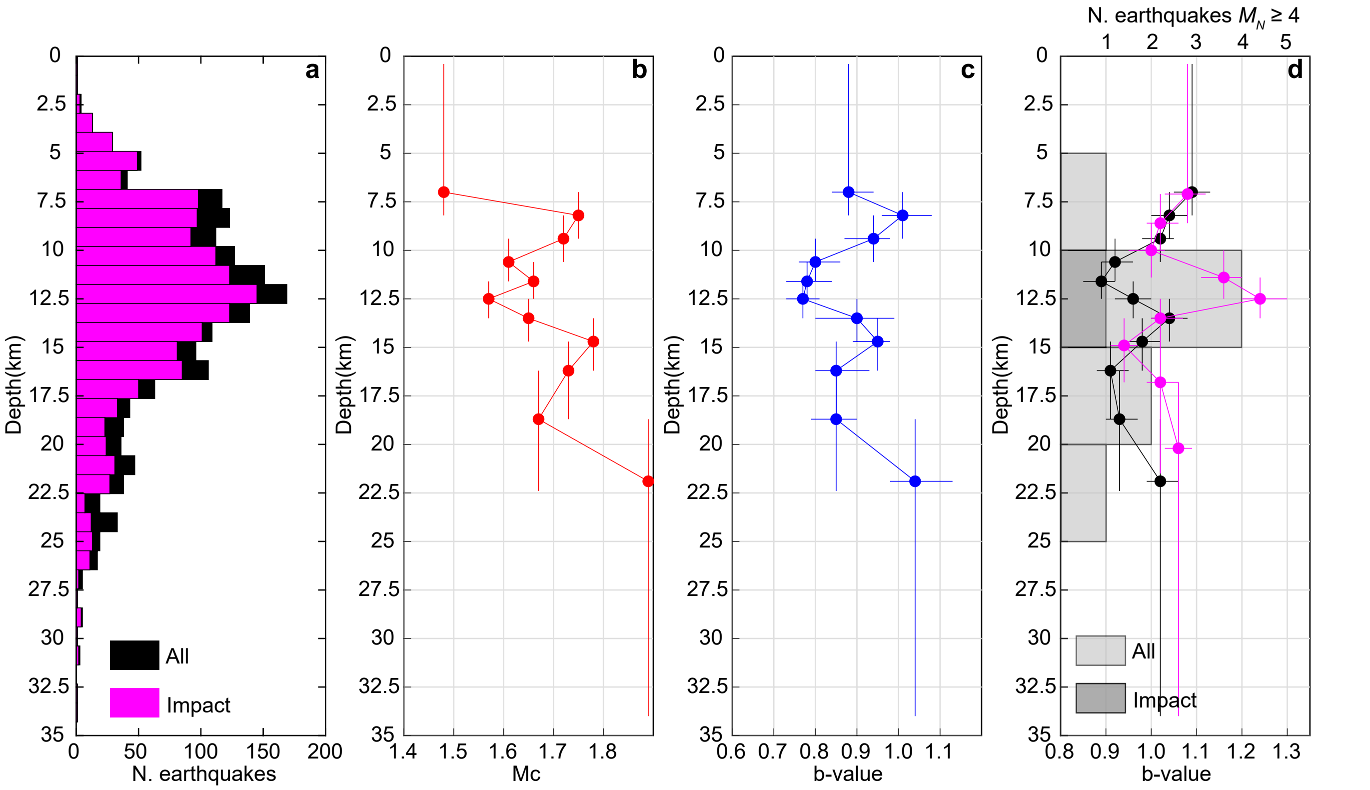

Figure 2. Magnitude-frequency distribution of relocated earthquakes in the CSZ. (a) Distribution of earthquakes with depth. (b) Depth-dependent variation of magnitude of completeness (Mc) calculated using moving windows of 300 events with 150-event overlap. (c) Depth-dependent b-value calculated using Mc in (b). (d) Depth-dependent b-value variation of using a fixed Mc = 1.86. Black points represent b-values for the entire catalog, magenta points indicate b-values for events within the impact structure. Grey bars indicate distribution of MN ≥ 4 events in the entire catalog (light) and within the events located inside the impact structure.

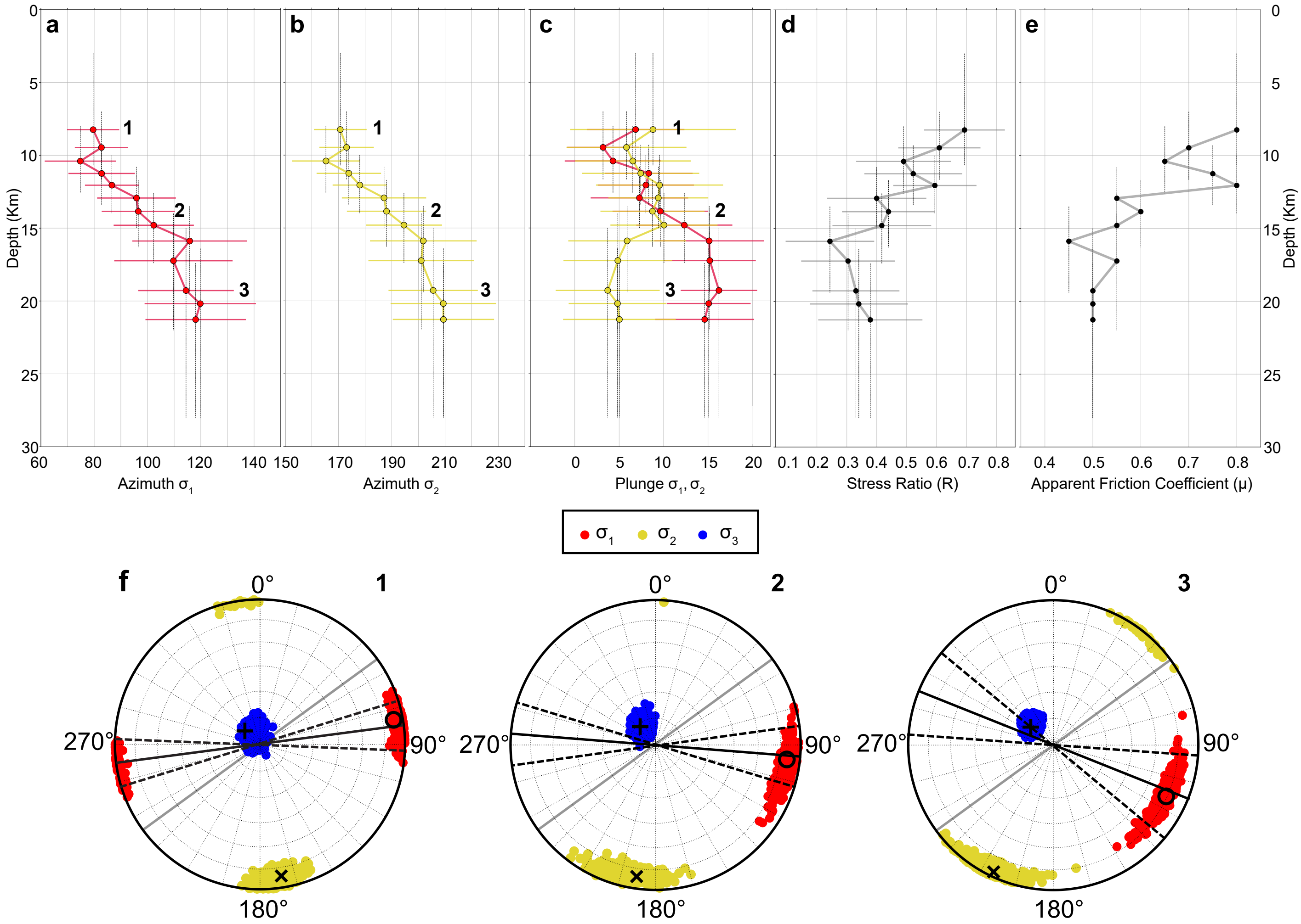

Figure 3. Depth-dependent variation of (a) σ_1 azimuth, (b) σ_2 azimuth, (c) σ_1 and σ_2 plunge, (d) stress ratio, and (e) apparent friction coefficient in moving windows of 75 events, overlapping by 15 events. Vertical lines represent depth range of the FMS used in each window, horizontal lines indicate 95% confidence interval. (f) Polar plots of specific stress inversions denoted by numbers (1-3). Black solid lines represent the orientation of the maximum horizontal stress (SHmax), with black dashed lines indicating 95% confidence interval limits of the. Grey solid lines represent the SHmax orientation from borehole breakouts (Mazzotti & Townend, 2010).

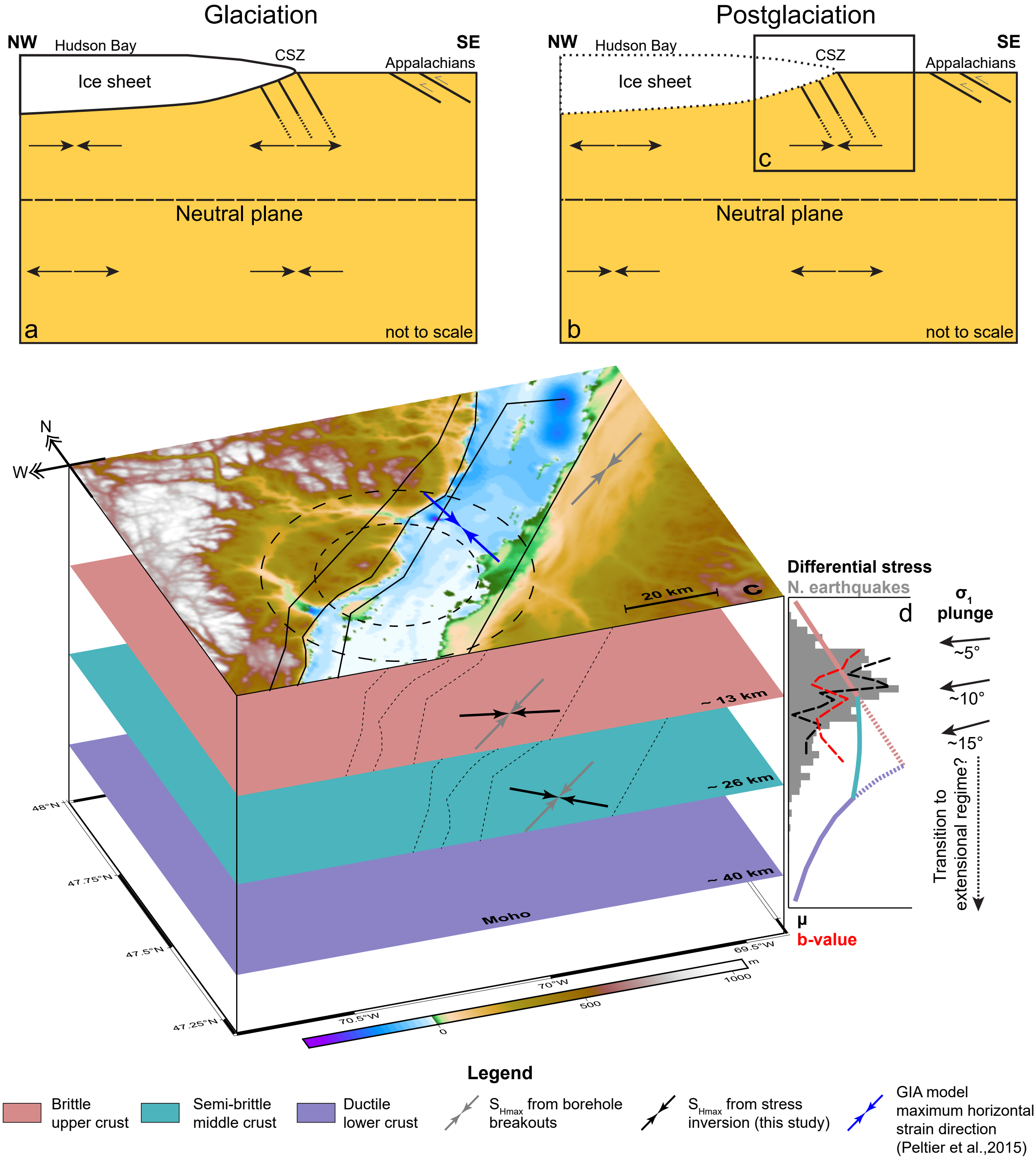

Figure 4. Schematic NW-SE cross section showing the expected horizontal stress distribution in the lithosphere during (a) glacial loading and (b) postglacial unloading following Wisconsin glaciation (85-11 kyr). (c) Conceptual model showing crustal depth-dependent clockwise rotation of maximum horizontal stress (SHmax) in the CSZ calculated here (black arrows) compared to SHmax from borehole breakouts data (grey arrows), and maximum horizontal strain direction from GIA modeling (Peltier et al., 2015). (d) Hypothetical rheological profile of the crust (solid lines color-coded by section of the crust) in the CSZ based on the distribution of earthquakes (grey histogram), b-value (dashed red line), apparent friction coefficient (μ) (dashed black line). Black arrows show the calculated rotation of the σ_1 plunge interpreted as possible transition to an extensional regime approaching the neutral plane (a, b). Vertical and horizontal axis do not have the same scale.

AGU PUBLICATIONS

Geophysical Research Letters

Supporting Information for

Depth-dependent crustal stress rotation and strength variation in the Charlevoix Seismic Zone (CSZ), Québec, Canada

A. Verdecchia[1], J. Onwuemeka[2], Y. Liu[2], and R. M. Harrington[1]

[1]Institute of Geology, Mineralogy and Geophysics, Ruhr-University Bochum, Bochum, Germany.

[2]Department of Earth and Planetary Sciences, McGill University, Montreal, Québec, Canada.

Contents of this file

Introduction

Here we provide a detailed methods description of the moment tensor inversion (Text S1), and additional details about the focal mechanism stress inversion (Text S2), and the coseismic stress changes modeling (Text S3) of the 1663 M 7.5 Charlevoix earthquake. Figure S1 shows a graphical representation of the *b*-values calculated for the entire relocated catalog and for groups of events inside and outside the impact structure. Figure S2 shows the new focal mechanism solutions used in this work in relation to pre-existing solutions from Mazzotti and Townend (2010). Figure S3 shows *b*-values for the entire relocated catalog calculated using magnitudes converted to M_w. Figure S4 supports the hypothesis that a previous large (M 7.5) earthquake in the CSZ has negligible effect on the current regional stress field. Finally, Figures S5 to S10 support the detailed description of the moment tensor inversion methodology from Text S1.

Text S1. Moment tensor inversion

The determination of fault plane solutions is particularly challenging in our study due to poor station coverage (see Figure S5). Although we use waveform data recorded by 11 seismic stations in the CSZ, most of the reported earthquakes are < M 3 with first arrivals exhibiting decreasing impulsive character with increasing source-to-station distance and decreasing event magnitude. The low (<6) number of impulsive first arrival pulses. especially for the smaller (<M

2.5) events, hinders the use of first-motion polarity to infer fault plane solutions. Hence, a full waveform modeling approach is preferred for computing full moment tensor solutions especially for events that do not have impulse first arrivals at available recording stations. We therefore use a probilistic, full waveform modeling algorithm, *Grond*, to invert full moment tensor solutions of 161 earthquakes (Heimann et al., 2018). *Grond* uses an amalgamation of time domain full waveform and cross-correlation, frequency domain amplitude spectra, and time domain envelopes in a Bayesian bootstrap-based probabilistic joint (centroid and moment tensor) inversion technique for source model optimization and uncertainty estimation. The overall uncertainty reflects misfits from each input data form. The joint inversion allows for time shifts to compensate for uncertainty in input velocity model. To avoid distortions due to, for example, incorrect transfer function and low signal-to-noise ratio (SNR), the bootstrap-based optimization performs user-defined independent, parallel runs to generate the final moment tensor solution. *Grond's* attributes makes it efficient for moment tensor inversion of small earthquakes recorded by sparse surface station networks with low SNR. We refer the reader to Heimann et al. (2018) for additional technical details.

Grond rapidly simulates earthquake waveforms for arbitrary source models from pre-computed Green's Function (GF) databases. We calculate the GF database with QSEIS (Wang, 1999) at a sampling rate of 20 Hz for surface receivers at epicentral distances and depths ranging from 0 - 150 km and 0.5 - 35 km, respectively, with spatial grid spacing of 0.1 km. The GF-database used here is managed by *Fomotso*, and can be downloaded from the Green's Mill web service at https://greens-mill.pyrocko.org/csz 20hz-855580 (last access: June 22, 2022). The 20 Hz sampling rate enables simulation of earthquake waveforms of up to 10 Hz (Nyquist), which is sufficient for moment tensor solutions of the magnitude range observed in this study. The optimum centroid moment tensor solution for each earthquake is determined as the solution with the lowest RMS from a suite of at least 40,000 trials. Each trial solution is results from the fitting of P and S waves in time and spectral domains.

Figure S6 shows focal mechanism solutions for 161 events, where each solution incorporates data from a minimum of 5, 3-component stations. The FMS of the largest event (06/03/2005 MN 4.6) located NE of the impact structure with depth of ~12 km suggests reverse fault motion on a NE-SW trending fault. A comparison of 4 MN > 3 event solutions reported by the Saint Louis University Earthquake Center (SLUEC) moment tensor catalog (SLUEC, 2018) shows similarity between solutions (Figure S7). The rotation angle between two double-couple focal mechanism solutions (Kagan angles) between our solutions and the SLUEC is < 15° (Figure S8), suggesting stable results. We perform an additional consistency check by calculating FMS of 25 events with impulsive first motions at more than 6 stations using *hybridMT* (Kwiatek et al., 2016) and also find consistent results (Figure S9). The Kagan angle of rotation of 84% of the focal mechanism solutions determined by *Grond* and *hybridMT* is less than 35° (Figure S10).

Text S2. Stress inversion

We use the *STRESSINVERSE* package implemented by Vavryčuk (2014) to invert for the principal stress directions. *STRESSINVERSE* applies an iterative procedure to select the nodal plane that is optimally oriented for failure in the estimated stress filed. The algorithm calculates the stress field orientation and the stress ratio in each iteration and selects the nodal plane with the large instability coefficient *I* for the next iteration. *I* is defined as:

$$I = \frac{\tau - \mu(\sigma - 1)}{\mu + \sqrt{1+\mu^2}},$$

where μ is the apparent coefficient of friction. The variables τ and σ are scaled shear and normal stresses, respectively.

We set $N_{noise\text{-}relatizations}$ = 500, $N_{noise\text{-}itarations}$ = 20, $N_{relatizations}$ = 10, $mean_{deviation}$ = 20 (see the associated User Guide available at https://www.ig.cas.cz/en/stress-inverse/). The mean inverted event depth is then used for depth information and for estimating the 95% confidence intervals for the inverted parameters from the 500 noise-realizations.

Text S3. Coseismic stress changes modeling of the 1663 M 7.5 Charlevoix earthquake

Following results from Ebel (2011), we use the software Coulomb 3.4 (Toda et al., 2011) to model a M 7.5 earthquake occurring on a 70 km-long and 15 km-wide thrust fault dipping to the south-east (Figure S4a). We used a heterogeneous slip distribution with a maximum slip of ~11 m located at the center of the fault at ~11 km depth. The resulting static stress drop is 21 MPa, in agreement with the stress drop values calculated for the CSZ (Onwuemeka et al., 2018).

References not included in the manuscript

Kwiatek, G., Martínez-Garzón, P., & Bohnhoff, M. (2016). Hybridmt: A matlab/shell environment package for seismic moment tensor inversion and refinement. *Seismological Research Letters*, 87 (4), 964-976.

Wang, R. (1999). A simple orthonormalization method for stable and efficient computation of green's functions. *Bulletin of the Seismological Society of America*, 89 (3), 733-741.

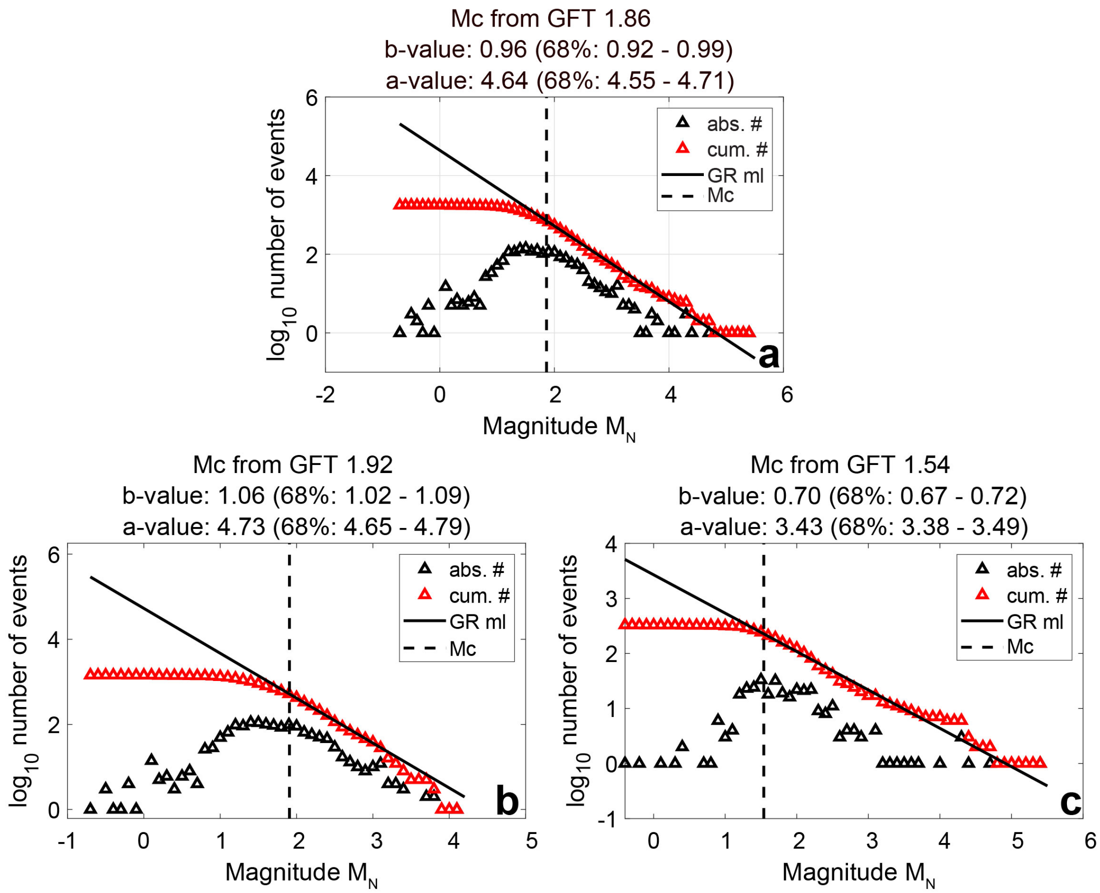

Figure S1. Frequency-magnitude distribution plots for the (a) entire relocated catalog, (b) earthquakes inside the impact structure, and (c) earthquakes outside the impact structure. The solid black lines represent the Gutenberg-Richet fit calculated using the maximum likelihood method (GR ml), while the vertical dashed lines represent the Mc values calculated using the Goodness-of-Fit test (GFT).

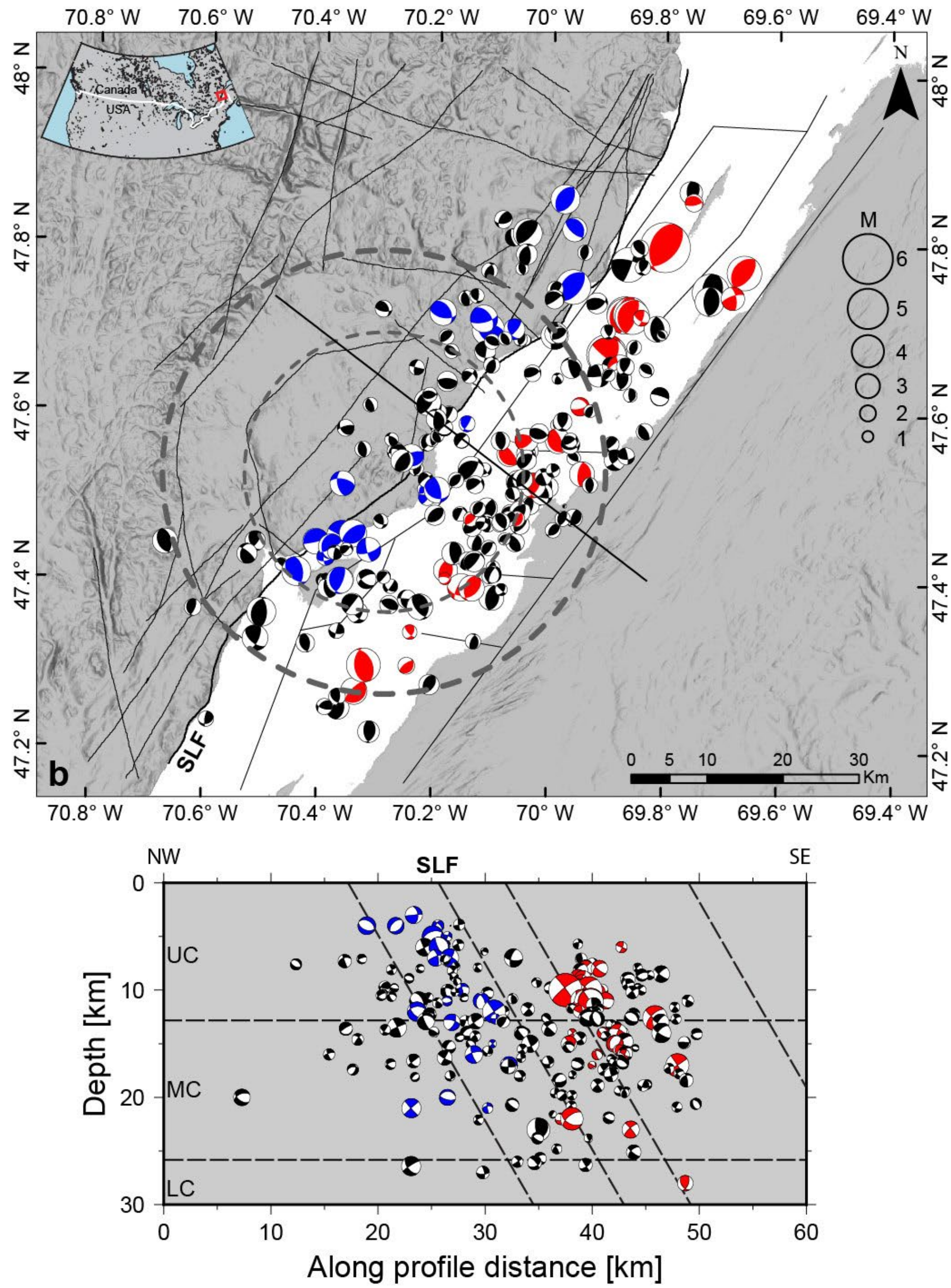

Figure S2. Map and relative cross-section of focal mechanism solutions used in this study. Blue and red FM solutions represent data from Mazzotti and Townend (2010), where blue FMs represent FMs northwest of the Saint-Laurent fault (SLF), and red FMs represent the FMs southeast of the SLF.

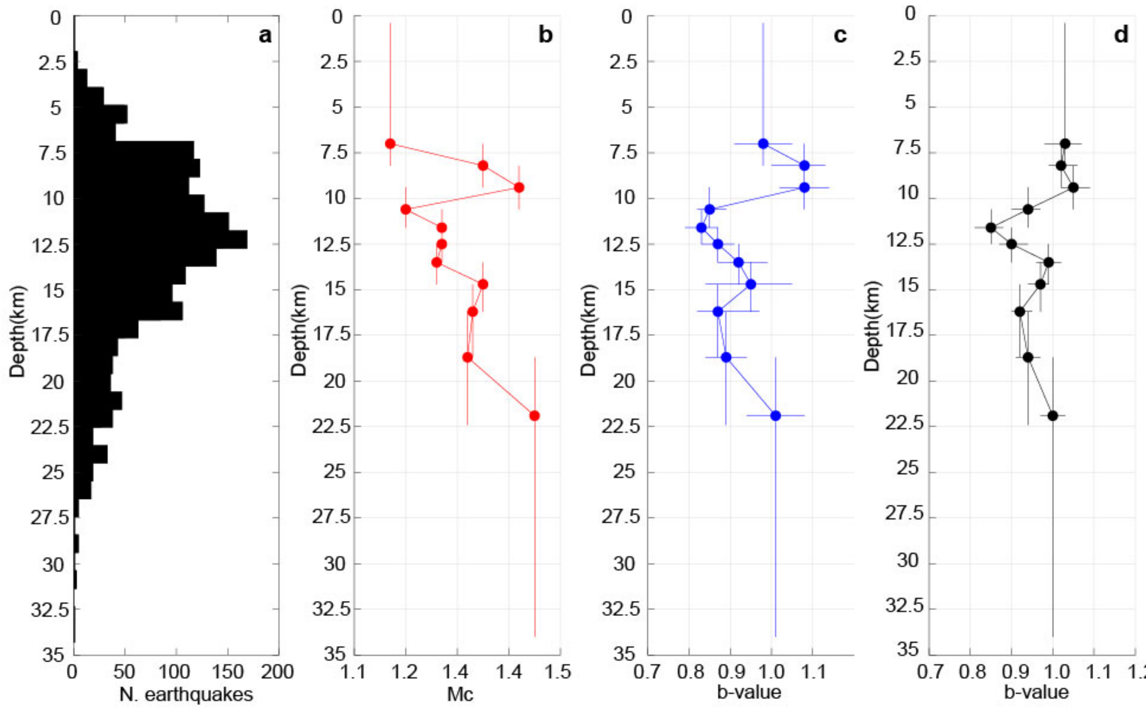

Figure S3. Magnitude-frequency distribution of relocated earthquakes in the CSZ using the catalog converted to M_W. (a) Distribution of earthquakes with depth. (b) Depth-dependent variation of magnitude of completeness (*Mc*) calculated using moving windows of 300 events with 150-event overlap. (c) Depth-dependent *b*-value variation calculated using *Mc* in (b). (d) Depth-dependent *b*-value variation calculated using a fixed *Mc* = 1.45.

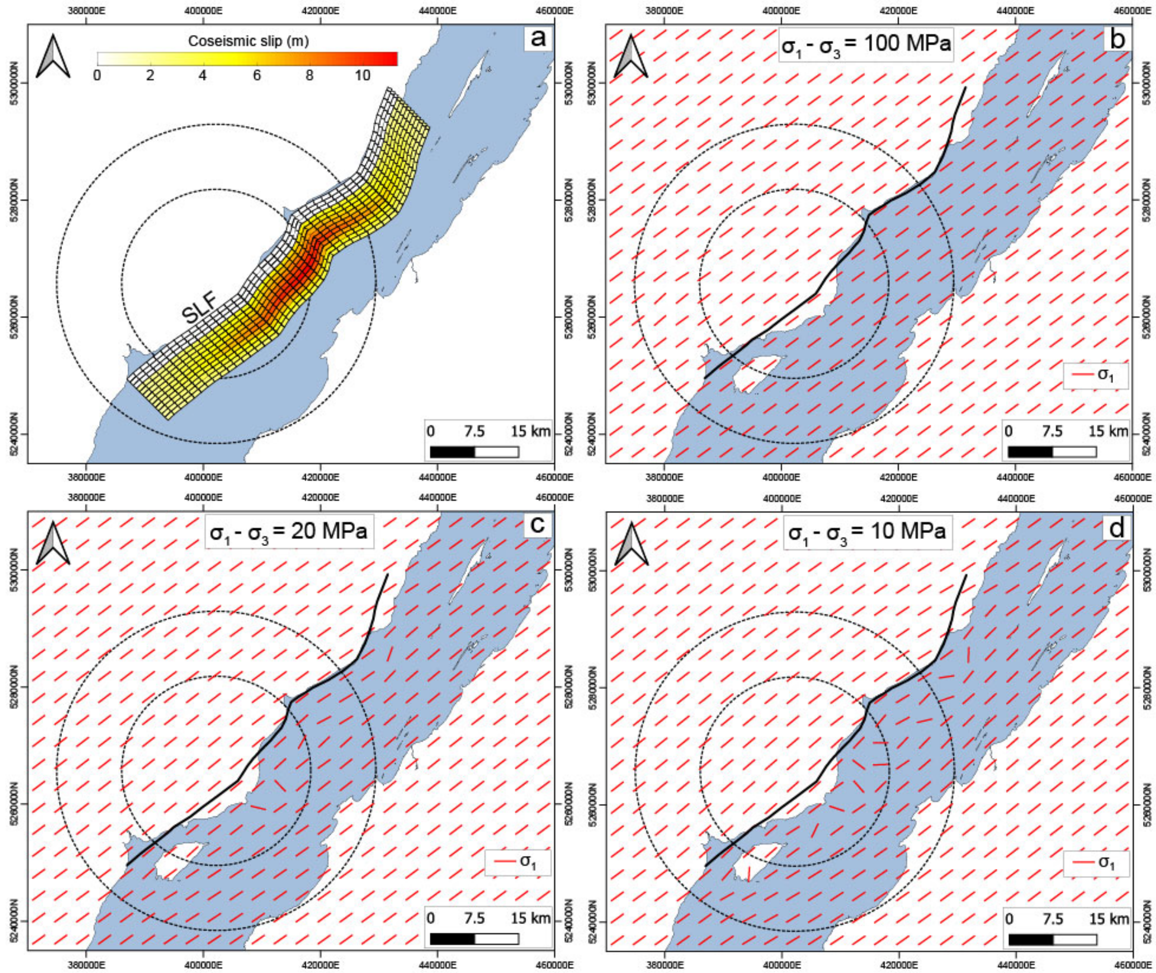

Figure S4. Modeled stress rotation due to coseismic slip of the 1663 Mw 7.5 Charlevoix earthquake calculated at 11 km depth. (a) Fault and slip model of the Saint Lawrence fault (SLF) used to calculate the stress rotation. Regional stress rotation calculated using (b) 100 MPa of background differential stress, (c) 20 MPa of background differential stress, and (d) 10 MPa of background differential stress. Dashed circles represent the Charlevoix meteorite impact structure.

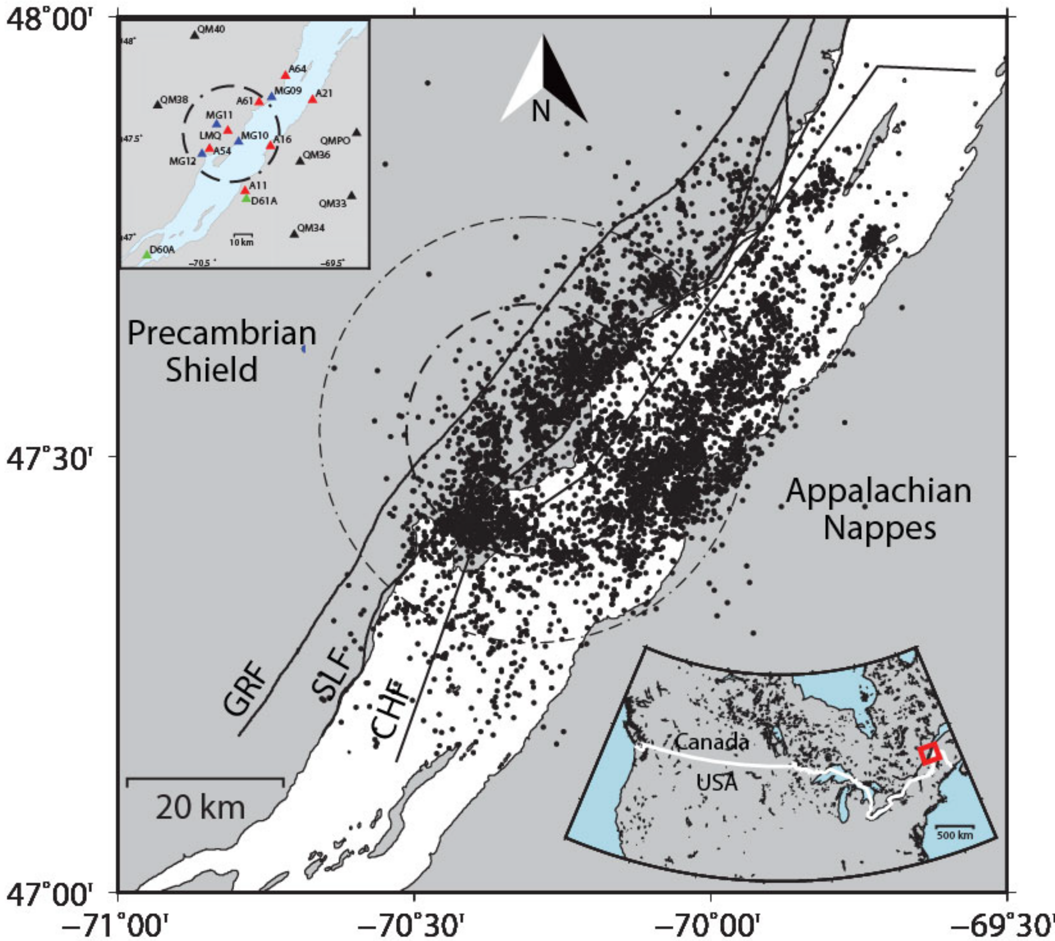

Figure S5. Distribution of 5663 earthquakes reported by Natural Resources Canada (NRCan) between January 1985 and May 2020. Dashed circle represent the Charlevoix meteorite impact structure. CHF, GRF, and SLF correspond to Charlevoix, Gouffre River, and St. Lawrence faults (Yu et al., 2016). Top-left inset: Broadband stations used in this study. Red, black, green and blue triangles represent CN, X8, TA and MG stations, respectively. Bottom-right inset: Red box represents the location of the study area.

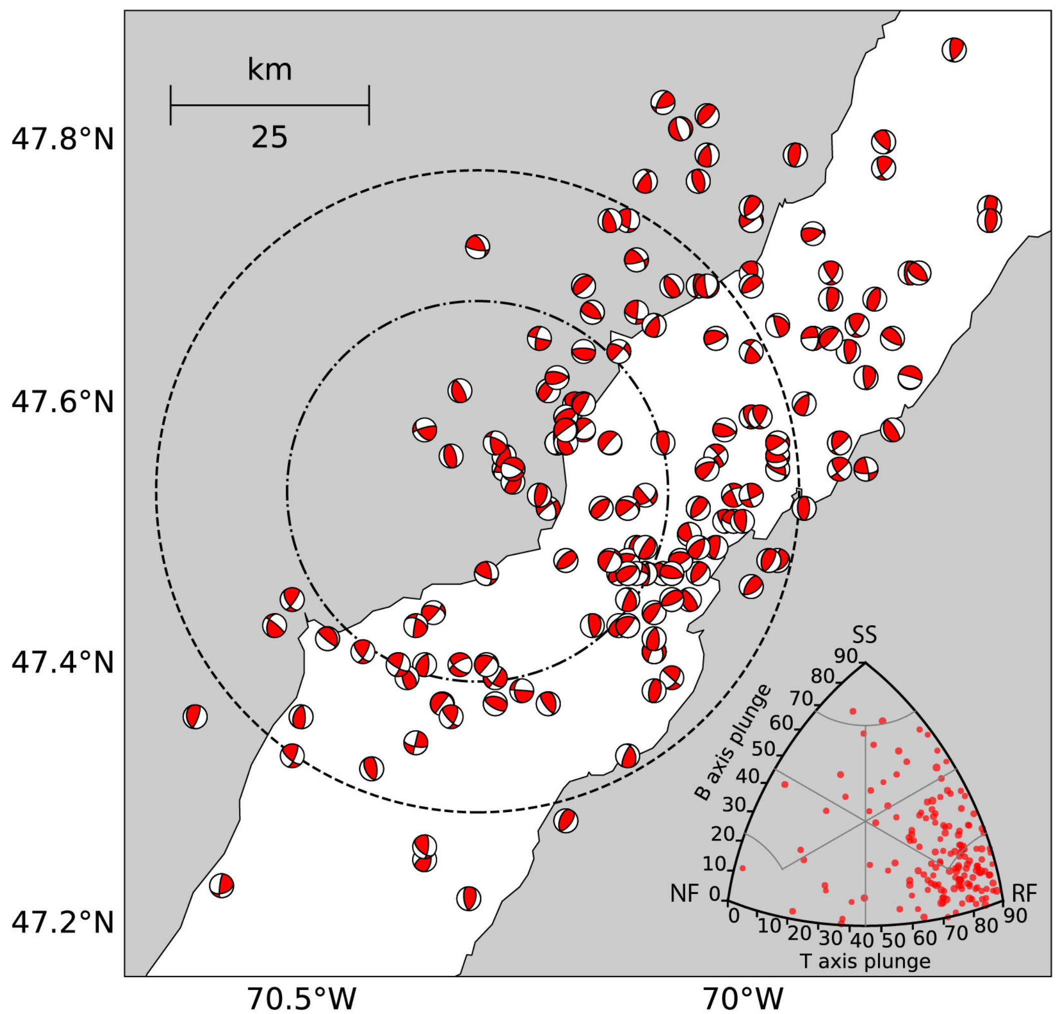

Figure S6. Focal mechanism (FM) solutions (161) computed with *Grond*. Bottom-right inset: Distribution of FM faulting style.

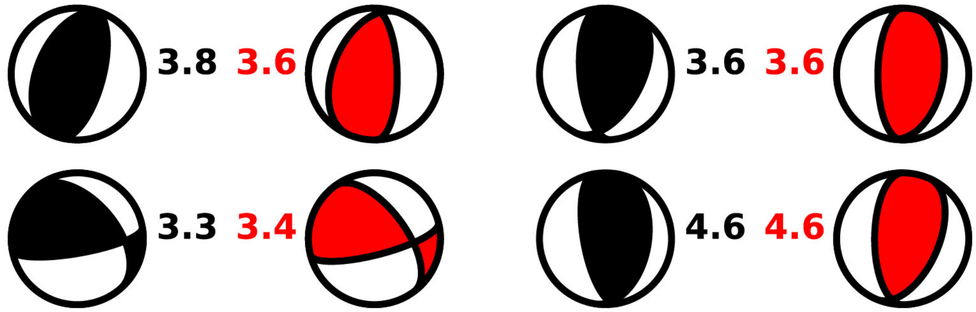

Figure S7. Comparison of FM solutions calculated here (red) and SLUEC catalog FMs (black) for 4 M 3+ events. The number beside each FM represent the moment magnitude estimated for the event.

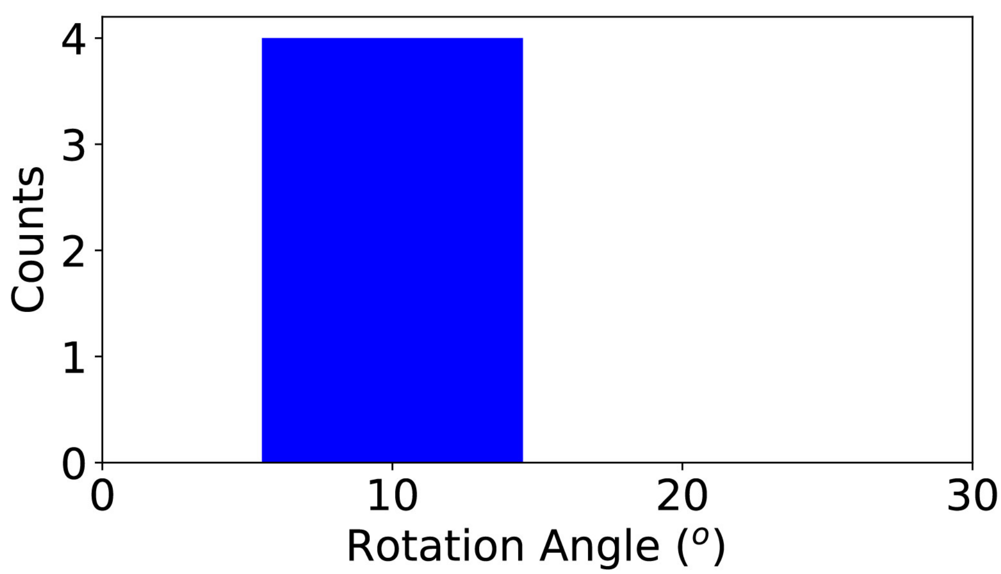

Figure S8. The Kagan angle of rotation between solutions calculated here and SLU catalog events shown in Figure S6.

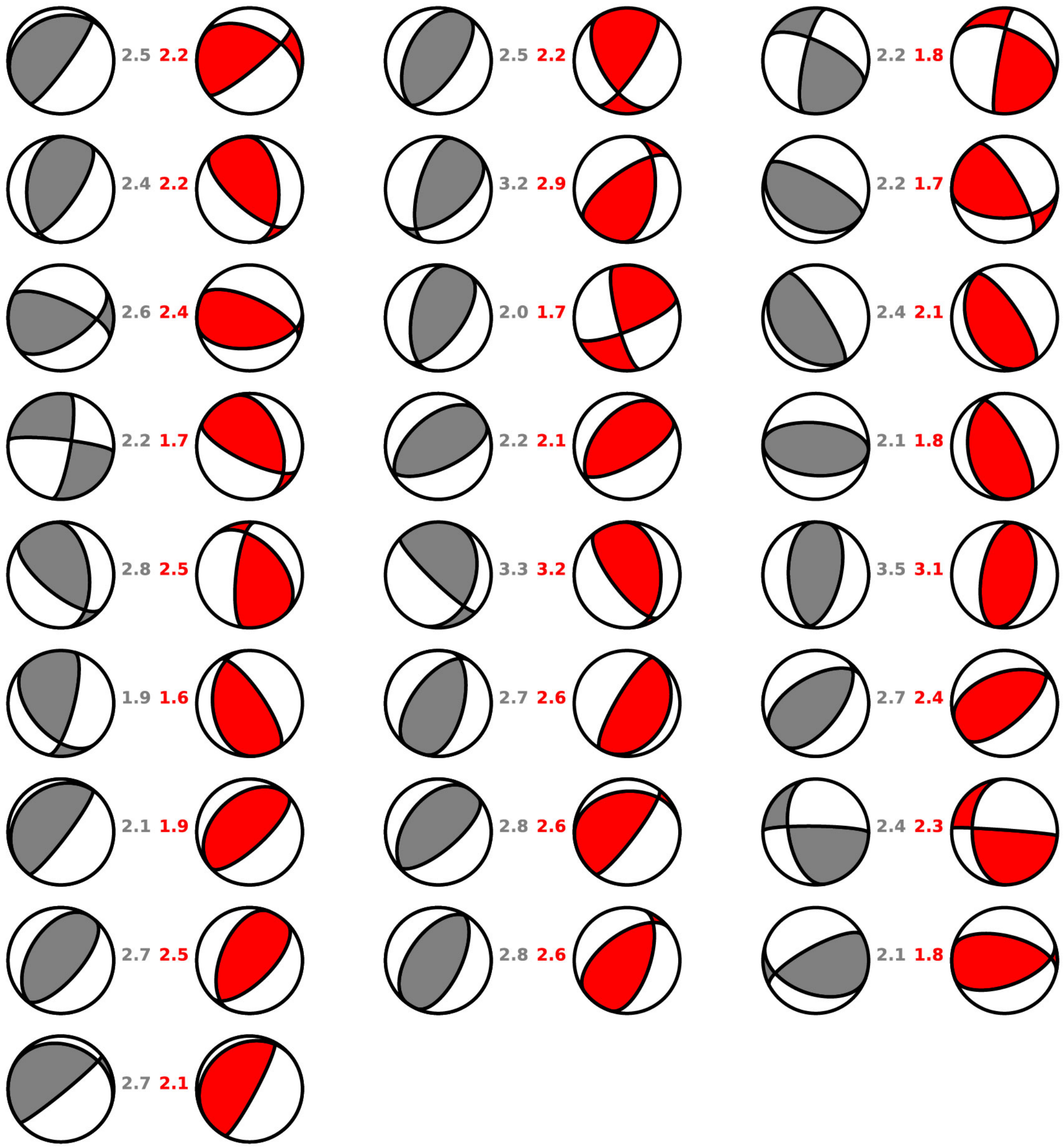

Figure S9. Comparison between 25 FM solutions determined with *Grond* (red) and *hybridMT* (gray). Estimated magnitude indicated next each FM in color corresponding to the method used.

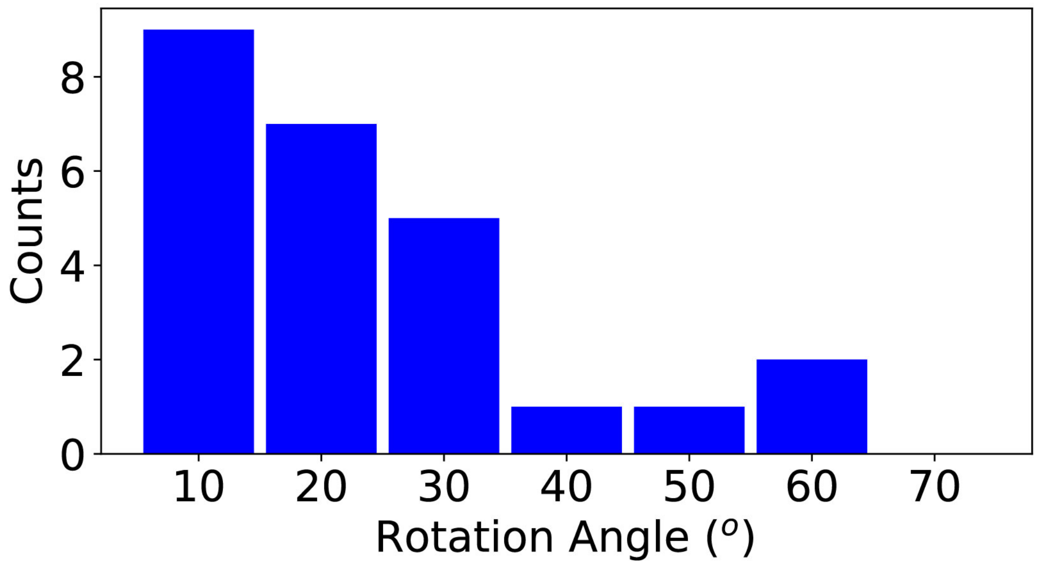

Figure S10. The Kagan angle of rotation between the two sets of solutions in Figure S8